nature research

https://doi.org/10.1038/s41565-020-00840-w

Supplementary information

Self-assembly of aramid amphiphiles into ultra-stable nanoribbons and aligned nanoribbon threads

In the format provided by the authors and unedited

Supplementary Information for

Self-assembly of aramid amphiphiles into ultra-stable nanoribbons and aligned nanoribbon threads

Ty Christoff-Tempesta, Yukio Cho, Dae-Yoon Kim, Michela Geri, Guillaume Lamour, Andrew J. Lew, Xiaobing Zuo, William R. Lindemann, Julia H. Ortony*

*Correspondence to: ortony@mit.edu

This PDF file includes:

S1. Synthesis and methods

S1a. Materials

Methyl 4-aminobenzoate (Sigma Aldrich, 98%), 3,3-dimethylbutyric acid (Sigma Aldrich, 98%), *N*,*N*-dimethyl-*p*-phenylenediamine (DPP, Sigma Aldrich, 97%), *N*-Boc-*p*-phenylenediamine (BPP, Sigma Aldrich, 97%), 1,3-propanesultone (PPS, Sigma Aldrich, 99%), 1,4-bis-Boc-1,4,7-triazaheptane (BBT, Chem Impex, 100%), diethylenetriamine-*N*,*N*,*N''*,*N''*-tetra-*tert*-butyl acetate-*N'*-acetic acid (DPTA, Combi Blocks, 95%), methoxypolyethylene glycol amine (Sigma Aldrich), 1-ethyl-3-(3-dimethylaminopropyl)carbodiimide hydrochloride (EDC, TCI Chemicals, 98%), 4-dimethylaminopyridine (DMAP, TCI Chemicals, 99%), 1-hydroxybenzotriazole hydrate (HOBt, TCI Chemicals, 97%), *N*,*N*-Diisopropylethylamine (DIPEA, Alfa Aesar, 99%), lithium hydroxide (LiOH, Alfa Aesar, 98%), sodium bicarbonate ($NaHCO_3$, Alfa Aesar, 99%), hydrochloric acid (HCl, Alfa Aesar, 36%), sodium sulfate (Na_2SO_4, Fisher Scientific, 99%), and trifluoroacetic acid (TFA, Alfa Aesar, 99%) were used as received without further purification.

S1b. Anionic amphiphile and its intermediates

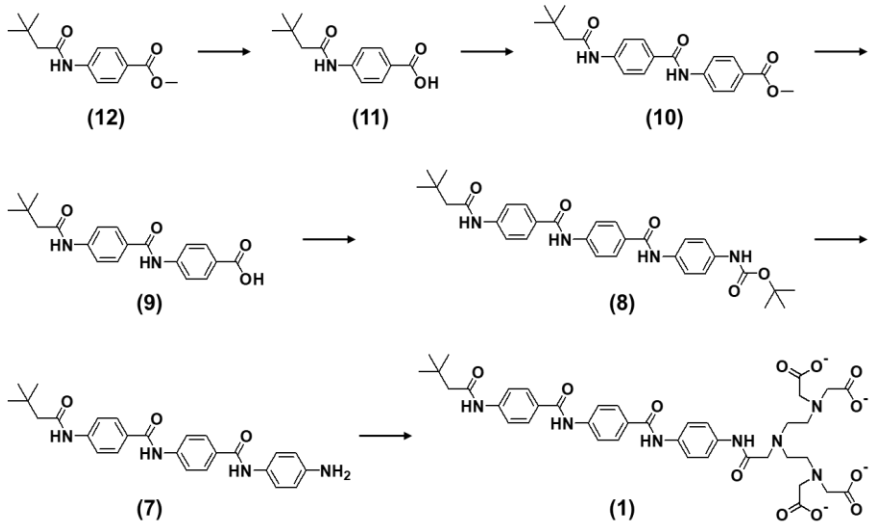

Supplementary Scheme 1. Synthesis scheme to obtain anionic amphiphile.

Methyl 4-(3,3-dimethylbutanamido)benzoate (**12**): A solution of methyl 4-aminobenzoate (11.01 mmol), 3,3-dimethylbutyric acid (16.52 mmol), EDC (33.03 mmol), and DMAP (33.03 mmol) in tetrahydrofuran (50 mL) was stirred at room temperature for 24 h. After the reaction, the solvent was removed in vacuum, and the residue was washed with distilled water and extracted in chloroform. The organic layer was purified by column chromatography with silica gel by using 1:1 ethyl acetate:hexane by volume (yield: 72%). ^{1}H NMR (400 MHz, DMSO-*d*): δ = 7.89 (d, 2H), 7.75 (d, 2H), 3.82 (s, 3H), 2.23 (s, 2H), 1.03 (s, 9H) ppm.

4-(3,3-dimethylbutanamido)benzoic acid (**11**): 10 M LiOH (10 mL) was added to a stirred solution of compound **12** (4.25 mmol) in ethanol (40 mL). The mixture was heated to 60°C and refluxed for 3 h, and then neutralized with an aqueous HCl solution. The precipitate was filtered off, and washed with water several times. The crude product was purified by reprecipitation from chloroform and methanol and dried under vacuum (yield: 98%). ^{1}H NMR (400 MHz, DMSO-*d*): δ = 7.87 (d, 2H), 7.72 (d, 2H), 2.23 (s, 2H), 1.03 (s, 9H) ppm.

Methyl 4-(4-(3,3-dimethylbutanamido)benzamido)benzoate (**10**): EDC (6.37 mmol), and DMAP (6.37 mmol) were added to a solution of compound **11** (2.13 mmol), and methyl 4-aminobenzoate (6.37 mmol) in dimethylformamide (30 mL). The solution was stirred for 24 h at 50 °C. After the reaction, the solvent was removed in vacuum, and the remaining residue was precipitated in water. The crude mixture was collected with filter flask. The filtered solid was washed with excess methanol and dried in vacuum (yield: 83%). ^{1}H NMR (400 MHz, DMSO-*d*): δ = 7.95 (m, 6H), 7.77 (d, 2H), 3.84 (s, 3H), 2.24 (s, 2H), 1.04 (s, 9H) ppm.

4-(4-(3,3-dimethylbutanamido)benzamido)benzoic acid (**9**): 10M LiOH (10 mL) was added to a stirred solution of compound **10** (2.55 mmol) in tetrahydrofuran (20 mL) and ethanol (10 mL). The mixture was refluxed for 6 h and then neutralized with an aqueous HCl solution. The precipitate was filtered off, washed with water, and dried under vacuum to afford the product (yield: 98%). ^{1}H NMR (400 MHz, DMSO-*d*): δ = 7.93 (m, 6H), 7.76 (d, 2H), 2.24 (s, 2H), 1.04 (s, 9H) ppm.

tert-Butyl 4-(4-(4-(3,3-dimethylbutanamido)benzamido)benzamido)phenylcarbamate (**8**): Into dimethylformamide (20 mL), compound **9** (0.85 mmol), BPP (2.55 mmol), EDC (2.55 mmol), and DMAP (2.55 mmol) were added. The well-dissolved solution was stirred at room temperature for 24 h. After solvent evaporation, the crude mixture was washed with water and methanol to give the desired white solid product (yield: 81%). ^{1}H NMR (400 MHz, DMSO-*d*): δ = 7.96 (m, 6H), 7.77 (d, 2H), 7.64 (d, 2H), 7.41 (d, 2H), 2.25 (s, 2H), 1.46 (s, 9H), 1.05 (s, 9H) ppm.

N-(4-(amino)phenyl)-4-(4-(3,3-dimethylbutanamido)benzamido)benzamide (**7**): TFA (500 μL) was added dropwise into the solution of compound **8** (0.55 mmol) in methylene chloride (15 mL). After stirring the mixture for 6 h at room temperature, the volatiles were distilled off and the remaining mixture was washed with saturated $NaHCO_3$ solution. The solid precipitate was filtered and dried in vacuum (yield: 99%). ^{1}H NMR (400 MHz, DMSO-*d*): δ = 7.95 (m, 6H), 7.75 (d, 2H), 7.48 (d, 2H), 6.72 (d, 2H), 2.25 (s, 2H), 1.05 (s, 9H) ppm.

2,2',2",2'"-((((2-((4-(4-(4-(3,3-dimethylbutanamido)benzamido)benzamido)phenyl)amino)-2-oxoethyl)azanediyl)bis(ethane-2,1-diyl))bis(azanetriyl))tetraacetate (**1**): A solution of compound **7** (0.29 mmol), DPTA (058 mmol), EDC (1.17 mmol), and DMAP (1.17 mmol) in dimethylformamide (20 mL) was stirred at 50 °C for 72 h. After the reaction, the solvent was removed in vacuum. The remaining residue was purified by flash column chromatography with silica gel by using 7:1 tetrahydrofuran : chloroform by volume as an eluent. The isolated compound was then reacted with TFA (500 μL) in methylene chloride (15 mL) for 48 h. The volatile fraction was removed under reduced pressure. Tetrahydrofuran was added to suspend the product and the product was collected by filtration (yield: 67%). ^{1}H NMR (400 MHz, DMSO-*d*): δ = 7.97 (m, 6H), 7.75 (m, 4H), 7.61 (d, 2H), 4.06 (s, 2H), 3.51 (s, 8H), 3.21 (t, 4H), 3.01 (t, 4H), 2.25 (s, 2H), 1.05 (s, 9H) ppm. ^{13}C NMR (400 MHz, DMSO-*d*): δ = 173.2, 170.9, 165.6, 165.1, 142.9, 135.7, 134.4, 128.9, 121.2, 119.8, 118.7, 55.1, 52.8, 50.1, 31.4, 30.1 ppm. MS (MALDI-ToF) m/z $[M + H]^+$ calculated: 820.34; $[M + H]^+$ found: 820.35.

S1c. Zwitterionic amphiphile and its intermediates

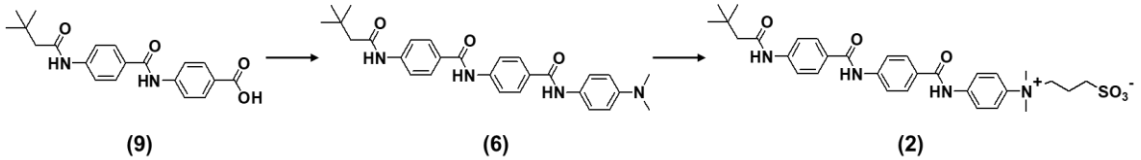

Supplementary Scheme 2. Synthesis scheme to obtain zwitterionic amphiphile.

N-(4-(dimethylamino)phenyl)-4-(4-(3,3-dimethylbutanamido)benzamido)benzamide (**6**): A solution of compound **9** (0.85 mmol), DPP (2.55 mmol), EDC (2.55 mmol), and HOBt (2.55 mmol) in

dimethylformamide (20 mL) was stirred at 50 °C for 24 h. After the reaction, the solvent was distilled off and the remaining residue was precipitated with water. The crude mixture was collected and washed with chloroform several times (yield: 78%). ^{1}H NMR (400 MHz, DMSO-*d*): δ = 7.95 (m, 6H), 7.77 (d, 2H), 7.57 (d, 2H), 6.73 (d, 2H), 2.88 (s, 6H), 2.25 (s, 2H), 1.05 (s, 9H) ppm.

3-((4-(4-(4-(3,3-dimethylbutanamido)benzamido)benzamido)phenyl)dimethylammonio)-propane -1-sulfonate (**2**): Compound **6** (1.85 mmol) was dissolved in dimethylformamide (15 mL) and tetrahydrofuran (15 mL). PPS (5 mL) was slowly injected using a syringe and the clear solution was stirred for 48 h in a sealed pressure tube at 70 °C. The volatile fraction was removed under reduced pressure and acetonitrile (50 mL) was added. The resulting precipitate was filtered and dried in vacuum (yield: 85%). ^{1}H NMR (400 MHz, DMSO-*d*): δ = 7.98 (m, 8H), 7.90 (d, 2H), 7.78 (d, 2H), 3.99 (m, 2H), 3.58 (s, 6H), 2.39 (t, 2H), 1.66 (m, 2H), 1.05 (s, 9H) ppm. ^{13}C NMR (400 MHz, DMSO-*d*): δ = 170.9, 165.8, 143.2, 140.9, 139.6, 129.1, 122.2, 121.1, 119.8, 118.7, 68.1, 54.4, 50.1, 47.9, 34.4, 30.1, 20.3 ppm. MS (MALDI-ToF) $[M + H]^+$ m/z calculated: 595.26; $[M + H]^+$ found: 595.41.

S1d. Cationic amphiphile and its intermediates

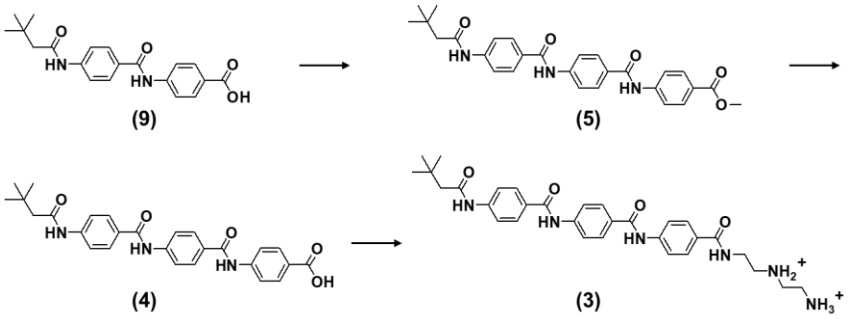

Supplementary Scheme 3. Synthesis scheme to obtain the cationic amphiphile.

Methyl 4-(4-(4-(3,3-dimethylbutanamido)benzamido)benzamido)benzoate (**5**): EDC (4.23 mmol) and DMAP (4.23 mmol) were added to a solution of compound **9** (1.41 mmol) and methyl 4-aminobenzoate (4.23 mmol) in dimethylformamide (20 mL). The solution was stirred for 24 h at 50 °C. After the reaction, the solvent was removed in vacuum, and the remaining residue was precipitated with water. The collected crude mixture was further washed with methanol and dried in vacuum (yield: 75%). ^{1}H NMR (400 MHz, DMSO-*d*): δ = 7.97 (m, 8H), 7.78 (d, 2H), 3.85 (s, 3H), 2.25 (s, 2H), 1.05 (s, 9H) ppm.

4-(4-(4-(3,3-dimethylbutanamido)benzamido)benzamido)benzoic acid (**4**): 10M LiOH (10 mL) was added to a stirred solution of compound **5** (1.05 mmol) in tetrahydrofuran (20 mL), and ethanol (10 mL). The mixture was refluxed for 12 h and then neutralized with an aqueous HCl solution to obtain a precipitate. The crude product was purified by reprecipitation with chloroform and ethanol and dried under vacuum (yield: 93%). ^{1}H NMR (400 MHz, DMSO-*d*): δ = 7.94 (m, 8H), 7.78 (d, 2H), 2.25 (s, 2H), 1.05 (s, 9H) ppm.

1-(2-(4-(4-(4-(3,3-dimethylbutanamido)benzamido)benzamido)benzamido)ethyl)ethane-1,2-diaminium (**3**): A solution of compound **4** (0.42 mmol), BBT (1.27 mmol), EDC (1.27 mmol), HOBt (1.27 mmol) and DIPEA (1.27 mmol) in dimethylformamide (20 mL) and dichloromethane (20 mL) was stirred at room temperature for 24 h. After the reaction, the solvent was removed in vacuum, and the remaining residue was washed with water several times. The isolated compound was then reacted with TFA (4 mL) in methylene chloride (40 mL) for 24 h. The volatile fraction was evaporated under reduced pressure. Diethyl ether was added to collect the product by filtration (yield: 85%). ^{1}H NMR (400 MHz, DMSO-*d*): δ = 7.98

(m, 10H), 7.76 (d, 2H), 3.58 (m, 2H), 3.39 (m, 2H), 3.13 (m, 4H), 2.25 (s, 2H), 1.04 (s, 9H) ppm. ^{13}C NMR (400 MHz, DMSO-*d*): δ = 171.1, 167.1, 165.7, 142.9, 129.1, 128.7, 128.4, 120.1, 119.4, 118.7, 50.1, 47.4, 44.6, 35.8, 31.4, 30.1 ppm. MS (MALDI-ToF) $[M + H]^+$ m/z calculated: 559.30; $[M + H]^+$ found: 559.29.

S1e. Synthesis of materials for Förster resonance energy transfer

Molecular exchange was measured by Förster resonance energy transfer (FRET) dark quenching when two nanoribbon populations, one containing a donor fluorophore and the other containing a dark quencher, were introduced into the same suspension. EDANS ((5-((2-aminoethyl)amino)naphthalene-1-sulfonic acid)) was used as the donor fluorophore and DABCYL (4-(dimethylaminoazo)benzene-4-carboxylic acid) was used as the dark quencher.

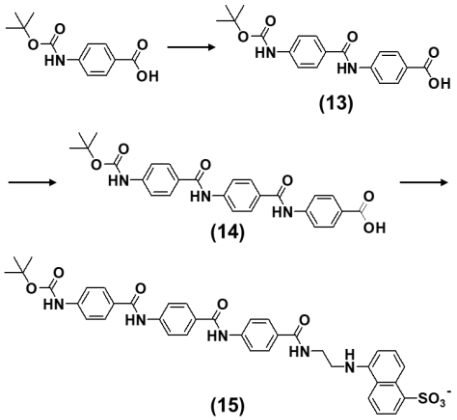

Supplementary Scheme 4. Synthesis scheme to obtain the EDANS-tagged amphiphile.

4-(4-(*tert*-Butoxycarbonyl)benzamido)benzoic acid (**13**): A solution of 4-(Boc-amino)benzoic acid (4.21 mmol), methyl 4-aminobenzoate (8.42 mmol), EDC (8.42 mmol), and DMAP (8.42 mmol) in chloroform (100 mL) were stirred at room temperature for 12 h. After the reaction, the solvent was evaporated under reduced pressure, and the remaining residue was precipitated with water. The mixture was filtered, and the precipitate was washed with methylene chloride several times. The solid material was dissolved in tetrahydrofuran (40 mL) and ethanol (20 mL). LiOH (21.1 mmol) in water (10 mL) was added to this solution, which was then refluxed at 70 °C for 3 h. The reaction mixture was shifted to room temperature and acidified to pH 2 with the addition of 5M HCl solution. The precipitate was collected by filtration and dried in vacuum (yield: 87%). ^{1}H NMR (400 MHz, DMSO-*d*): δ = 7.93 (m, 6H), 7.66 (d, 2H), 1.49 (s, 9H) ppm.

4-(4-(4-(*tert*-Butoxycarbonyl)benzamido)benzamido)benzoic acid (**14**): A solution of compound **13** (2.11 mmol), methyl 4-aminobenzoate (4.22 mmol), EDC (4.22 mmol), and DMAP (4.22 mmol) were in dimethylformamide (30 mL) was stirred at room temperature for 24 h. After the reaction, the solvent was distilled off, and the remaining residue was washed with water and methanol. The solid material was dissolved in tetrahydrofuran (20 mL) and ethanol (10 mL). LiOH (10.5 mmol) in water (10 mL) was added to this solution, which was then refluxed at 70 °C for 6 h. The reaction mixture was shifted to room temperature and acidified to pH 2 with the addition of 5M HCl solution. The precipitate was collected by filtration and dried in vacuum (yield: 82%). ^{1}H NMR (400 MHz, DMSO-*d*): δ = 7.95 (m, 10H), 7.67 (d, 2H), 1.49 (s, 9H) ppm.

EDANS-tagged amphiphile, 5-((2-(4-(4-(4-(3,3-dimethylbutanamido)benzamido)benzamido) benzamido)ethyl)amino)naphthalene-1-sulfonic acid (**15**): A solution of compound **14** (0.21 mmol), EDC (0.25 mmol), and DMAP (0.25 mmol) in dimethylformamide (10 mL) was stirred for 30 min. EDANS (0.25 mmol) was then added into the solution and the solution was stirred for 24 h at room temperature. Water

was poured into the solution to yield a precipitate, which was obtained by filtration and washed with chloroform (yield: 64%). ^{1}H NMR (400 MHz, DMSO-*d*): δ = 8.02 (m, 1H), 7.97 (m, 10H), 7.62 (d, 2H), 7.34 (m, 4H), 6.57 (d, 1H), 3.85 (m, 1H), 3.43 (m, 2H), 3.16 (m, 2H), 1.51 (s, 9H) ppm. MS (MALDI-ToF) $[M + H]^+$ m/z calculated: 723.23; $[M + H]^+$ found: 723.24.

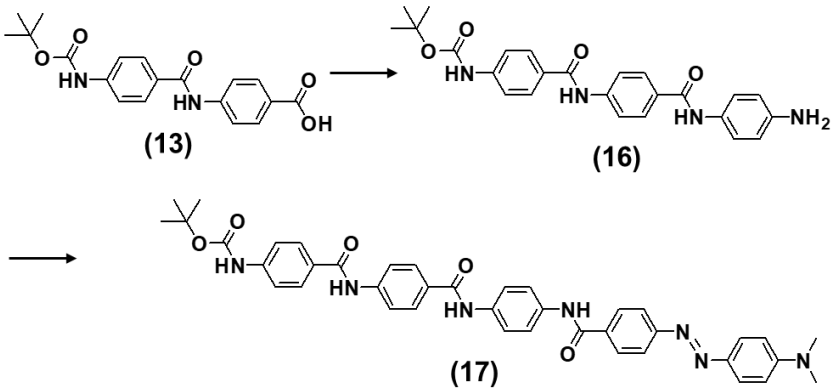

Supplementary Scheme 5. Synthesis scheme to obtain the DABCYL-tagged amphiphile.

tert-Butyl 4-((4-((4-aminophenyl)carbamoyl)phenyl)carbamoyl)phenylcarbamate (**16**): A solution of compound **13** (0.56 mmol), 1,4-diaminobenzene (11.22 mmol), EDC (0.67 mmol), and DMAP (0.67 mmol) in dimethylformamide (80 mL) was stirred at 25 °C for 24 h. The volatile fraction was removed under reduced pressure and the remaining residues were washed several times with methanol and filtered to obtain the product (yield: 59%). ^{1}H NMR (400 MHz, DMSO-*d*): δ = 7.92 (m, 6H), 7.60 (d, 2H), 7.36 (d, 2H), 6.54 (d, 2H), 4.91 (s, 2H), 1.51 (s, 9H) ppm.

DABCYL-tagged amphiphile, (E)-4-((4-(dimethylamino)phenyl)diazenyl)-N-(4-(4-(4-(3,3-dimethylbutanamido)benzamido)benzamido)phenyl)benzamide (**17**): A solution of compound **16** (0.67 mmol), DABCYL (0.81 mmol), EDC (0.81 mmol), and DMAP (0.81 mmol) in dimethylformamide (10 mL) was stirred at 25 °C for 48 h. The solvent was then evaporated under reduced pressure. The crude mixtures were purified with water and chloroform and filtered to obtain the product (yield: 71%). ^{1}H NMR (400 MHz, DMSO-*d*): δ = 7.94 (m, 12H), 7.62 (d, 4H), 7.45 (d, 2H), 6.66 (d, 2H), 3.10 (s, 6H), 1.51 (s, 9H) ppm. MS (MALDI-ToF) $[M + Na]^+$ m/z calculated: 720.29; $[M + Na]^+$ found: 720.30.

S1f. Oligo(ethylene glycol) amphiphile

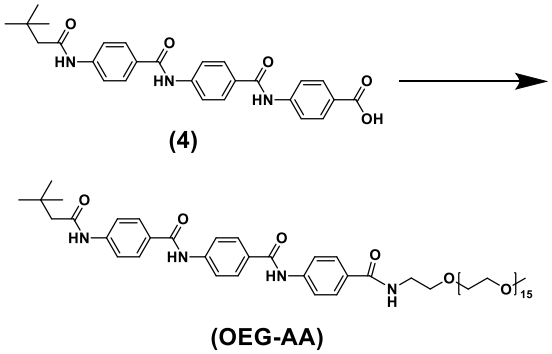

Supplementary Scheme 6. Synthesis scheme to obtain the oligo(ethylene glycol) amphiphile.

N-(4-((2,5,8,11,14,17,20,23,26,29,32,35,38,41,44,47-hexadecaoxanonatetracontan-49-yl)carbamoyl)phenyl)-4-(4-(3,3-dimethylbutanamido)benzamido)benzamide (**OEG-AA**): A solution of compound **4** (0.1 mmol), methoxypolyethylene glycol amine (M_w = 750 g/mol, 0.2 mmol), EDC (0.2 mmol), and HOBt (0.2 mmol) in dimethylformamide (10 mL) was stirred at rt for 24 h. The solvent was then evaporated under reduced pressure and the remaining residue was dissolved in dichloromethane. The solution was washed by ice water twice via solvent extraction and the organic fraction in dichloromethane was retained. The final product in dichloromethane was obtained by removing the solvent under reduced pressure and lyophilizing the remaining semi-solid (yield: 62%). ^{1}H NMR (400 MHz, DMSO-*d*): δ = 7.97 (m, 6H), 7.84 (m, 2H), 7.76 (d, 2H), 7.49 (d, 2H), 3.51 (s, 70H), 2.25 (m, 2H), 1.05 (s, 9H) ppm.
Major peak: MS (MALDI-ToF) $[M + Na]^+$ m/z calculated for n = 15 is 1213.64; $[M + Na]^+$ Found: 1213.61
Minor peak: MS (MALDI-ToF) $[M + Na]^+$ m/z calculated for n = 13 is 1125.58; $[M + Na]^+$ Found: 1125.56
Minor peak: MS (MALDI-ToF) $[M + Na]^+$ m/z calculated for n = 14 is 1169.61; $[M + Na]^+$ Found: 1169.59
Minor peak: MS (MALDI-ToF) $[M + Na]^+$ m/z calculated for n = 16 is 1257.66; $[M + Na]^+$ Found: 1257.64
Minor peak: MS (MALDI-ToF) $[M + Na]^+$ m/z calculated for n = 17 is 1301.69; $[M + Na]^+$ Found: 1301.67

S2. Chemical characterization

S2a. Nuclear magnetic resonance

Proton (^{1}H) and carbon (^{13}C) nuclear magnetic resonance (NMR) measurements were performed on a Bruker Avance III DPX 400. 20 mg of sample were dissolved in 500 µL deuterated dimethylsulfoxide (DMSO-*d*) for analysis. The chemical shifts were measured in parts per million (ppm) down-field from tetramethylsilane. Self-assembly behavior was also modulated and studied by addition of deuterated water to the DMSO-*d* solutions, as discussed with Supplementary Figs. 16-18.

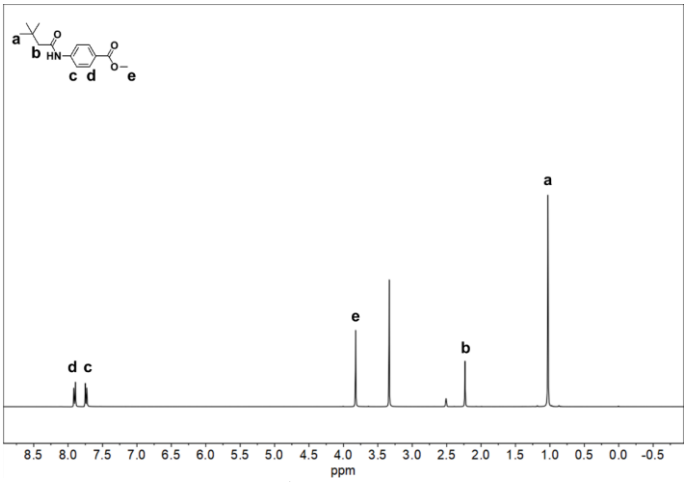

Supplementary Fig. 1. ^{1}H NMR spectra of compound **12**.

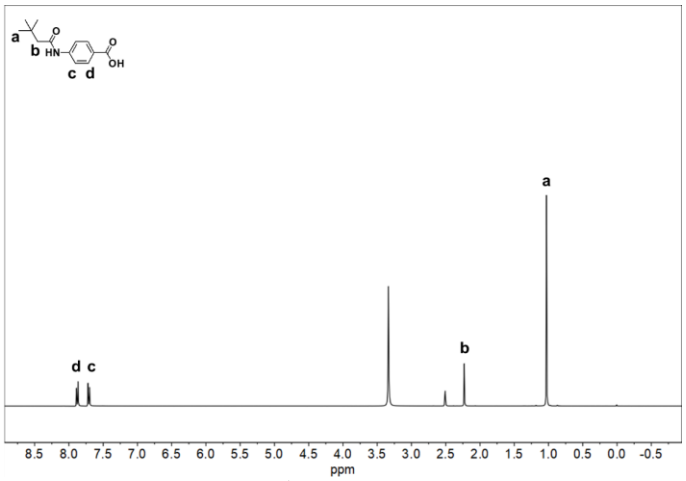

Supplementary Fig. 2. ^{1}H NMR spectra of compound **11**.

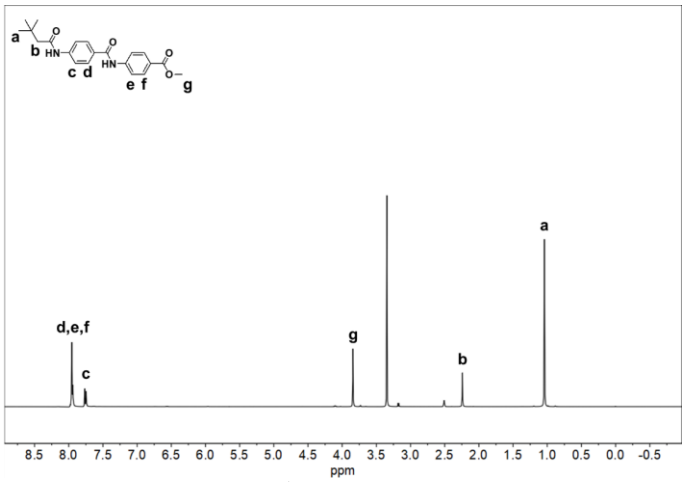

Supplementary Fig. 3. ^{1}H NMR spectra of compound **10**.

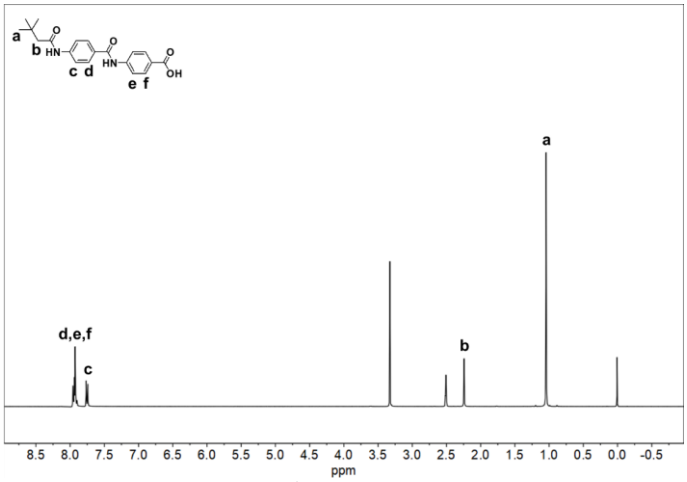

Supplementary Fig. 4. ^{1}H NMR spectra of compound **9**.

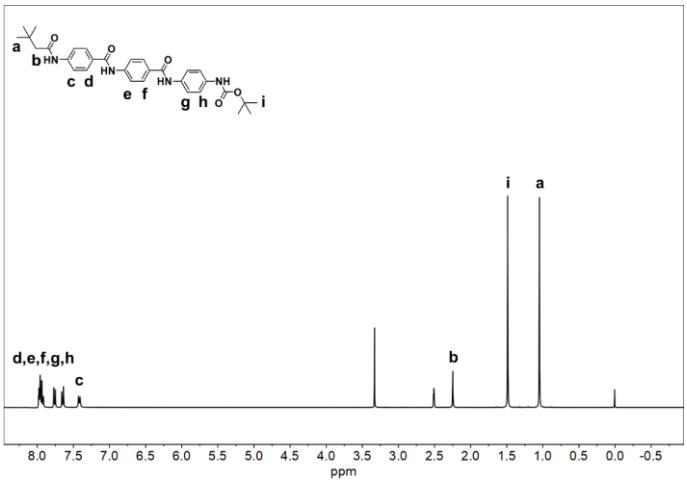

Supplementary Fig. 5. ^{1}H NMR spectra of compound **8**.

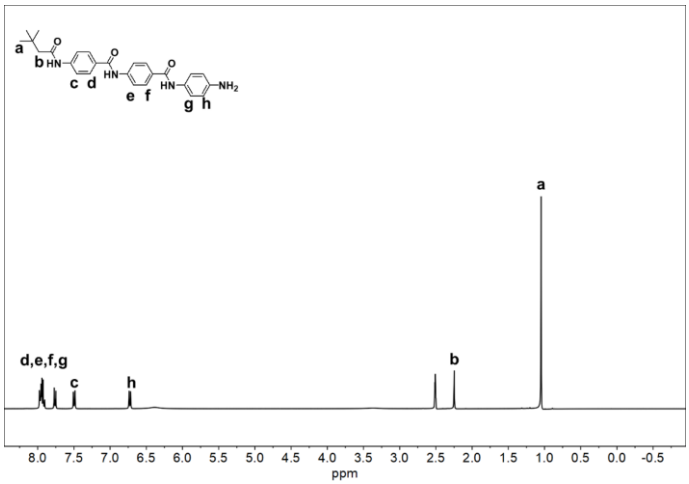

Supplementary Fig. 6. ^{1}H NMR spectra of compound **7**.

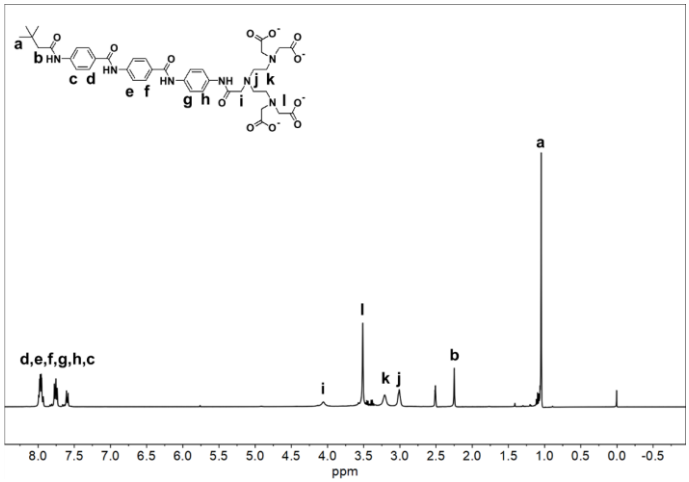

Supplementary Fig. 7. ^{1}H NMR spectra of compound **1**.

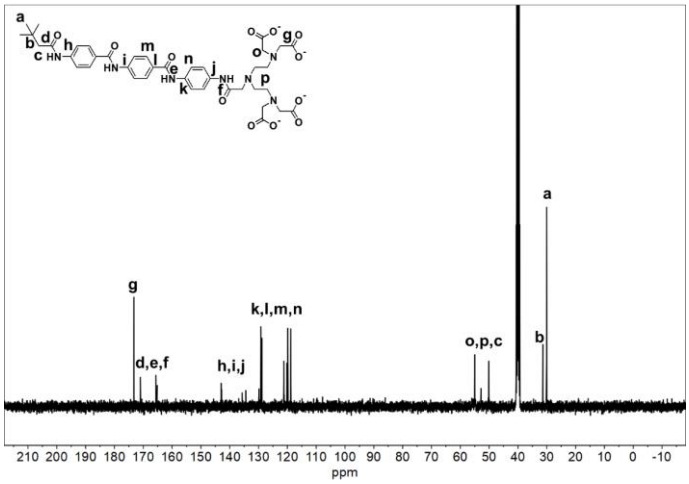

Supplementary Fig. 8. ^{13}C NMR spectra of compound **1**.

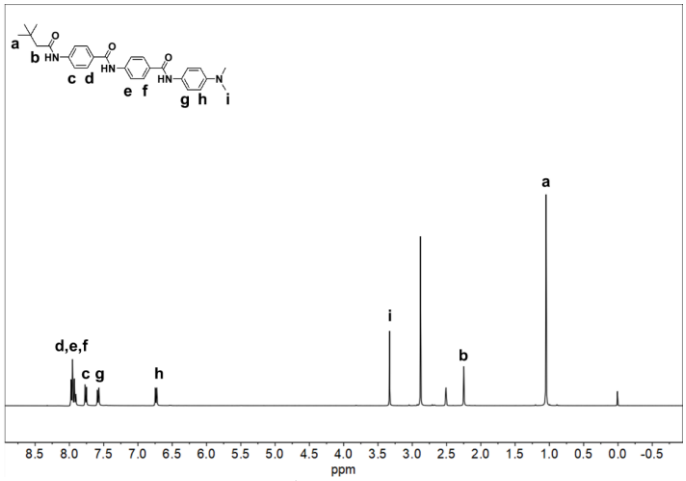

Supplementary Fig. 9. ^{1}H NMR spectra of compound **6**.

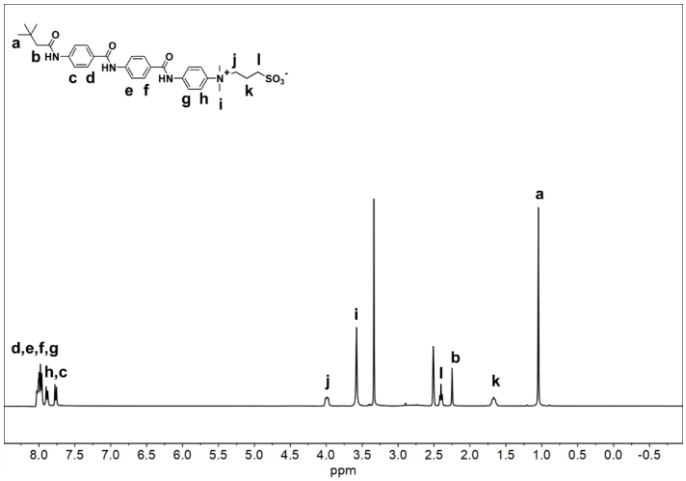

Supplementary Fig. 10. ^{1}H NMR spectra of compound **2**.

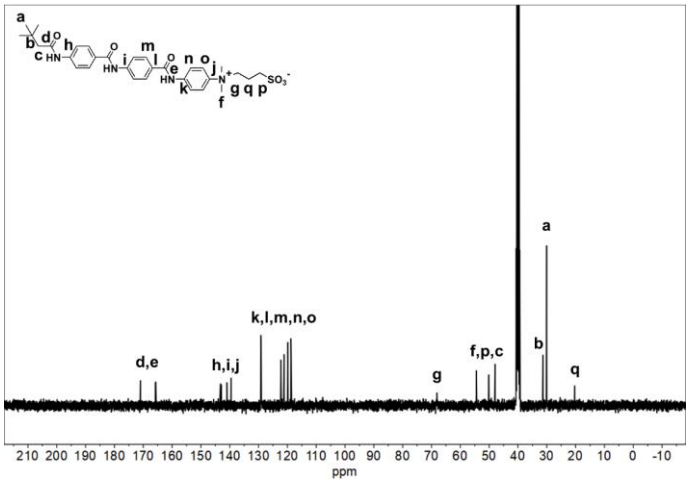

Supplementary Fig. 11. ^{13}C NMR spectra of compound **2**.

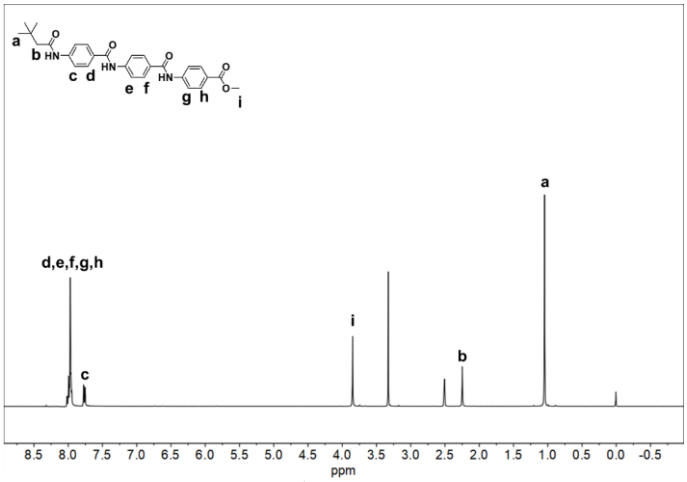

Supplementary Fig. 12. ^{1}H NMR spectra of compound **5**.

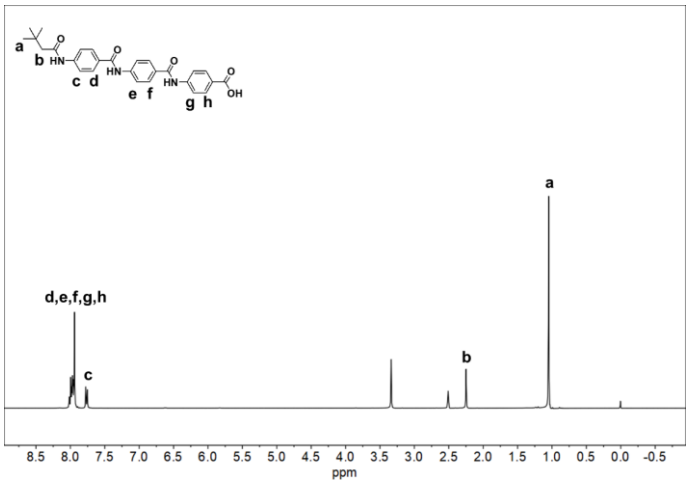

Supplementary Fig. 13. ^{1}H NMR spectra of compound **4**.

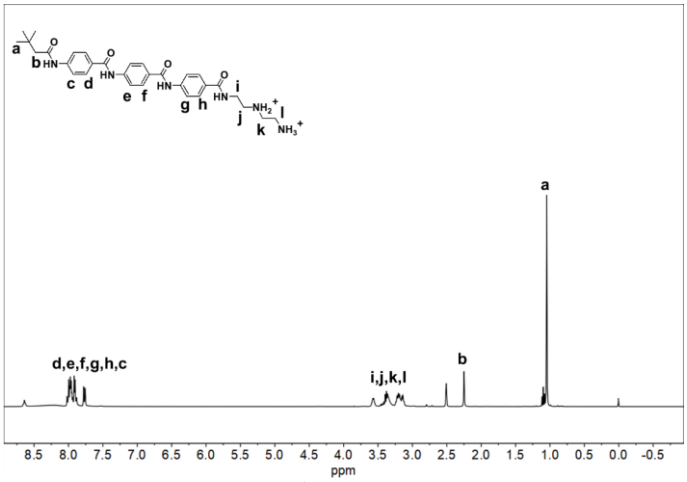

Supplementary Fig. 14. ^{1}H NMR spectra of compound **3**.

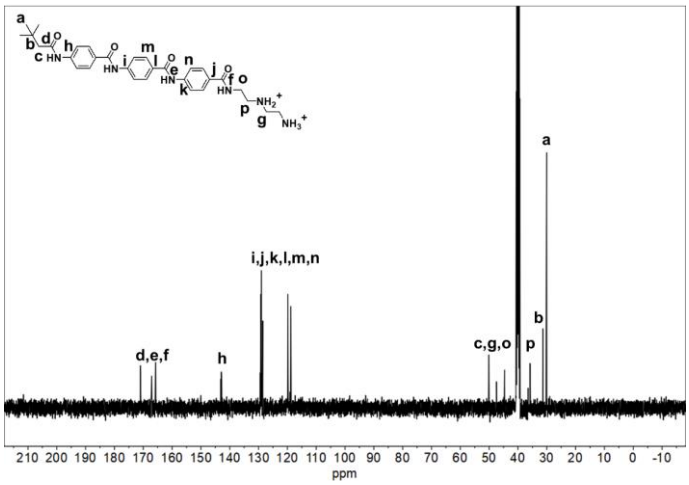

Supplementary Fig. 15. ^{13}C NMR spectra of compound **3**.

Solvent effects: The self-assembly behavior of aramid amphiphiles can be mediated by solvent variation as shown in Supplementary Figs. 16-18. In good solvent, such as DMSO-*d*, the ^{1}H NMR spectrum of aramid amphiphile samples indicate a monomeric state with well-resolved sharp peaks corresponding to aromatic protons between δ = 8.1 and 7.5 ppm. The aromatic proton peaks broaden as aggregation occurs when D_2O is titrated into the solution. The broadening of the aromatic H_1 and H_2 peaks is concomitant with the formation of strong intermolecular interactions upon self-assembly. The simultaneous upfield shift of protons is observed when small intermolecular distances induce a magnetic shielding effect. The broadening of the aromatic proton peaks is consistent with slowing of conformational dynamics within the nanostructures as assembly occurs with increasing D_2O concentrations. Compound **3** exhibits enhanced NMR signal at higher D_2O concentrations due to its higher solubility in D_2O than compounds **1** and **2**. No nanoribbons or other assemblies of compound **3** are observed in conventional TEM when a grid is prepared from the sample of 100% DMSO-*d*.

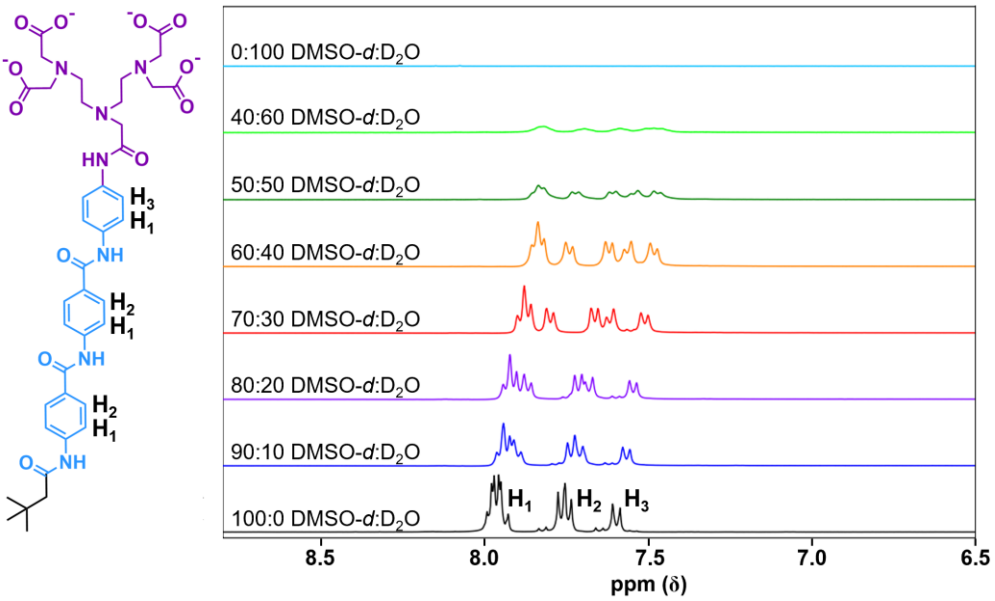

Supplementary Fig. 16. ^{1}H NMR spectra of compound **1** in DMSO-*d* with increasing D_2O content.

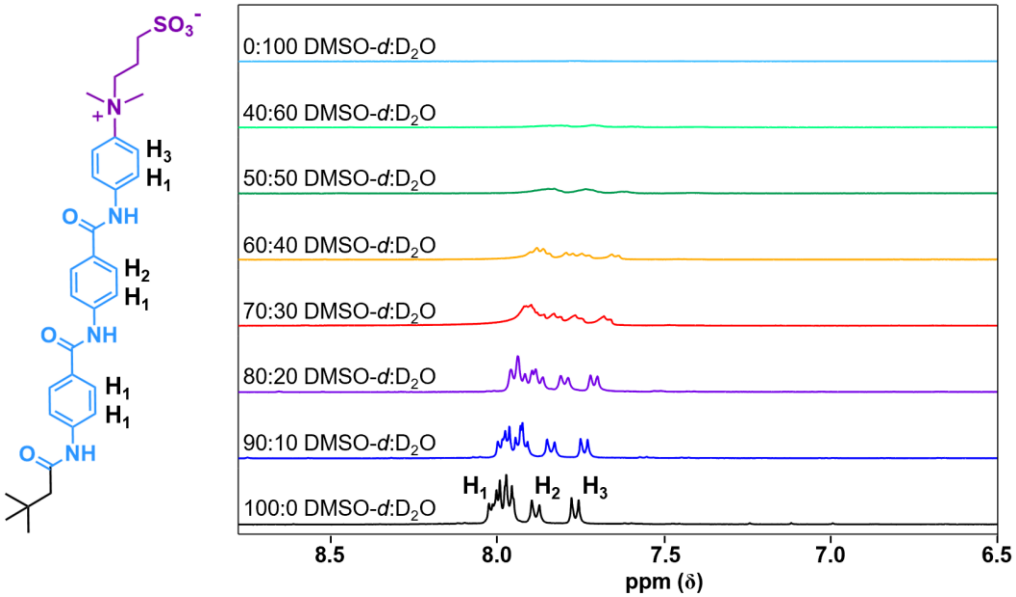

Supplementary Fig. 17. ^{1}H NMR spectra of compound **2** in DMSO-*d* with increasing D_2O content.

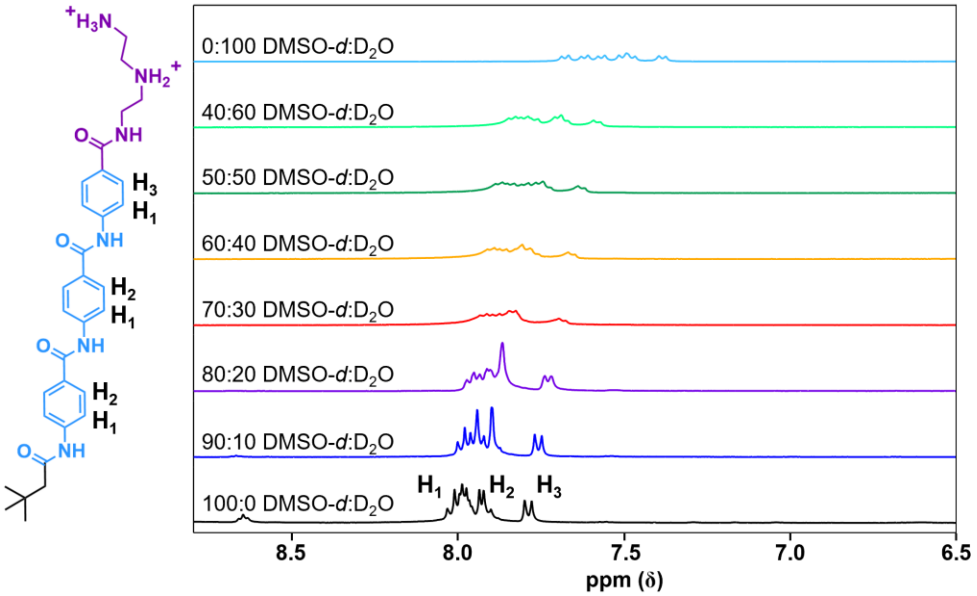

Supplementary Fig. 18. ^{1}H NMR spectra of compound **3** in DMSO-*d* with increasing D_2O content.

S2b. Mass spectrometry

Molecular weights of amphiphiles were determined using a Bruker Omniflex matrix assisted laser desorption/ionization-time-of-flight (MALDI-ToF) instrument with a Reflectron accessory. A matrix solution was prepared by adding 15 mg of *α*-cyano-4-hydroxycinnamic acid to 1 mL of 1:1 water:acetonitrile by volume with 0.1% TFA, vortexing for one minute, centrifuging for 20 s, and retaining the supernatant. 10 µL of 1 mg/mL amphiphile in water was then transferred into a centrifuge tube and diluted with the matrix solution to a 50 pmol/µL concentration. 1 µL of a 1 mg/mL calibrant solution (SpheriCal Peptide Low, Polymer Factory) in tetrahydrofuran was added to the solutions as an internal calibrant. 2 µL of each mass spectrometry solution was pipetted and dried onto a sample plate for analysis.

S2c. Attenuated total reflectance Fourier-transform infrared spectroscopy

ATR-FTIR spectra of compound **3** were captured across systematically varying concentrations of DMSO-*d* and D_2O to characterize hydrogen bonding between amphiphiles. The results of this study with powder control samples of compound **3** and compound **4**, a synthesis intermediate with no head group, are shown in Supplementary Fig. 19.

Characteristic β-sheet hydrogen bonding is commonly investigated via amide I vibration shifting around 1650 cm^{-1}.[37] Two peaks are observed in this region at 1672 and 1652 cm^{-1} for the compound **3** powder (unassembled) sample. The peak at 1672 cm^{-1} is not observed for compound **4**, which lacks the amide bond that couples the amphiphile head group to the aramid structural domain. Therefore, we assign the peak at 1672 cm^{-1} to the C = O stretch of the amide bond between the head group and structural domain and 1652 cm^{-1} to the C = O stretch of the amide bonding in aramid structural domain. We observe the peak at 1672 cm^{-1} is present among all mixtures of DMSO-*d* and D_2O. Conversely, the amide I peak shifts to 1638 cm^{-1} in the full D_2O environment. This red shift indicates hydrogen bonding formation between at the corresponding amide bonding when compound **3** assembles in D_2O.[38] The peak at 1600 cm^{-1} is attributed to C – C stretching in the aromatic rings and is constant over all spectra.

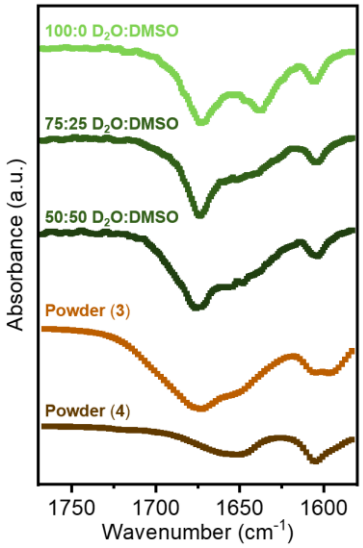

Supplementary Fig. 19. FTIR spectra of compounds **3** and **4** in dried powder form as controls and compound 3 dissolved in varying ratios of DMSO-*d* to D_2O.

Supplementary Fig. 20 shows the effect of bath sonication time on ATR-IR spectra of compound **3** dissolved in different solvent mixtures of DMSO-*d* and D_2O. Broadly, the peak at 1638 cm^{-1} is enhanced with longer sonication times and lower levels of DMSO-*d*. We attribute this sharpening to increasing uniformity of intermolecular hydrogen bonding distances upon sonication.

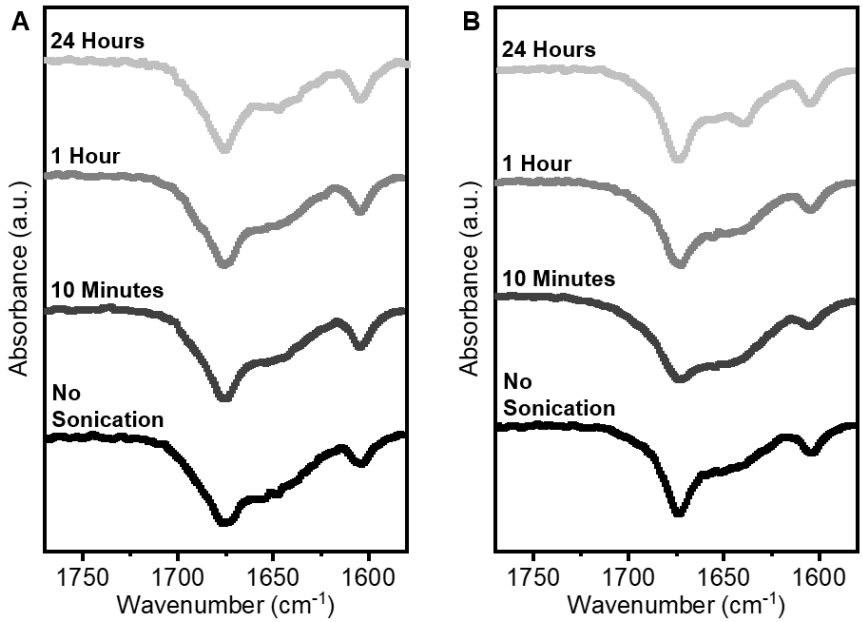

Supplementary Fig. 20. ATR-IR spectra showing the effect of sonication time on intermolecular interactions between compound **3** in (**A**) a 50:50 mixture of D_2O:DMSO-*d* and (**B**) a 75:25 mixture of D_2O:DMSO-*d*. The amide I bond at 1638 cm^{-1} is enhanced with higher proportions of water and longer sonication times, resulting from the formation of a more uniform hydrogen bonding network in the self-assembled system.

S3. Structural characterization

S3a. Transmission electron microscopy

Conventional transmission electron microscopy (TEM) of nanoribbons formed by self-assembly of **1**, **2**, and **3** are shown in Supplementary Fig. 21.

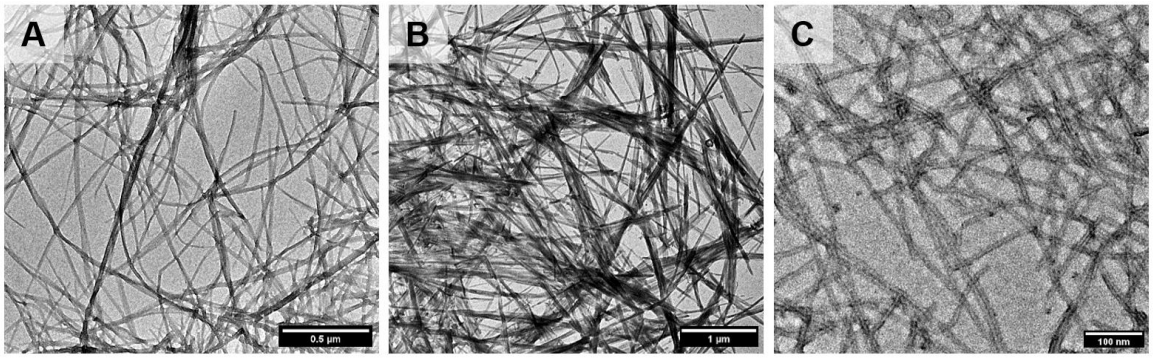

Supplementary Fig. 21. TEM images of assemblies of compounds (**A**) **1**, (**B**) **2**, and (**C**) **3**.

Changing the environment pH can modulate assembly morphology by changing the effective head group charge and size of amphiphiles. Aqueous suspensions of compounds **1**, **2**, and **3** at 0.1 mg/mL concentrations were adjusted to pH 3 and pH 11 using 0.5 M hydrochloric acid and sodium hydroxide, respectively, and bench sonicated for 10 minutes to investigate the effect of pH on assembly morphology. Compound **1** forms disordered aggregates at pH 3 and short noodle-like assemblies at pH 11; compound **2** forms needle-like assemblies at pH 3 and disordered aggregates at pH 11; and compound **3** forms cylindrical nanotubes at pH 3 and plate-like aggregates at pH 11. Representative micrographs showing these structures are shown in Supplementary Fig. 22.

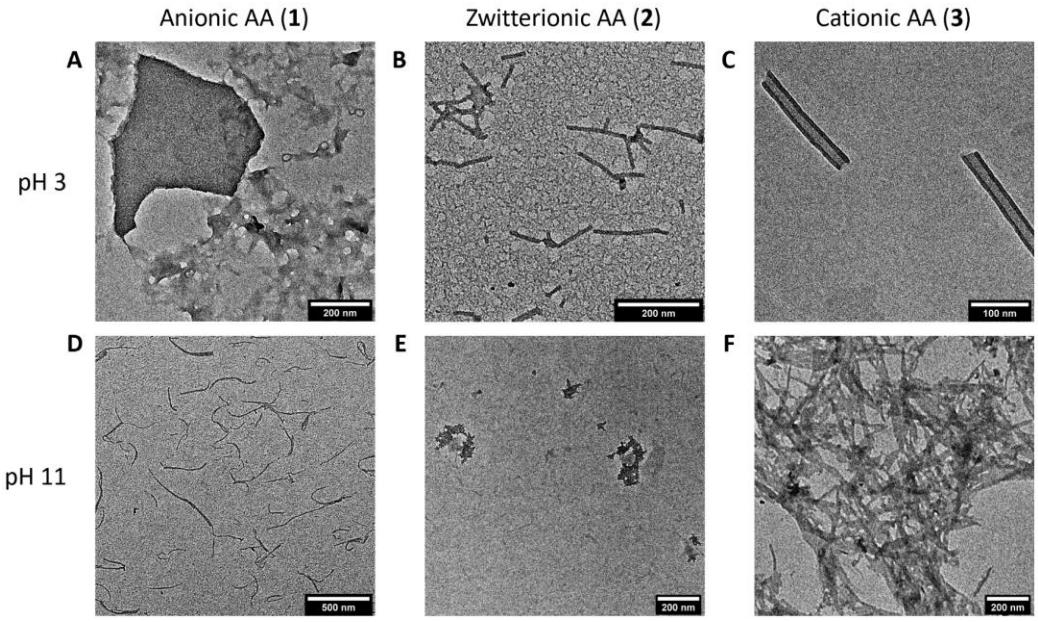

Supplementary Fig. 22. The self-assembly morphology of aramid amphiphiles can be modulated by changing the pH. Representative micrographs of (**A**) compound **1** at pH 3, (**B**) compound **2** at pH 3, (C) compound **3** at pH 3, (**D**) compound **1** at pH 11, (**E**) compound **2** at pH 11, and (**F**) compound **3** at pH 11 are shown here.

S3b. Cryogenic transmission electron microscopy

Supplementary Fig. 23 shows cryo-TEM micrographs of nanoribbons of compounds **1**, **2**, and **3**, respectively. Fig. 23a shows that bundling of **1** occurs, likely due to inter-ribbon hydrogen bonding of the head groups. Interestingly, self-assembly of **2** leads to both high-aspect-ratio nanoribbons and in some cases, complete nanoribbon circles. Nanoribbon widths in Cryo-TEM for **1**, **2**, and **3** nanoribbons are measured as 5.5 nm, 5.1 nm, and 5.8 nm, respectively for n = 25 measurements with approximately 5% error.

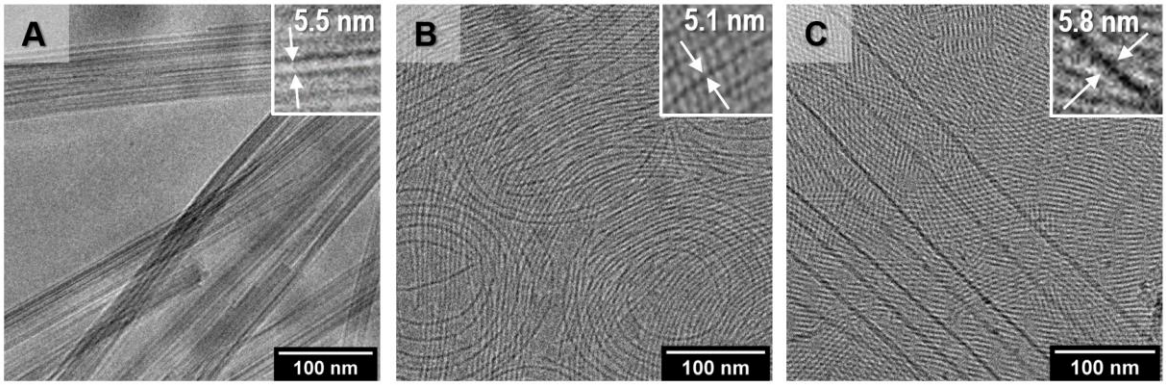

Supplementary Fig. 23. Cryo-TEM images of assemblies of compounds (**A**) **1**, (**B**) **2**, and (**C**) **3**.

Supplementary Fig. 24 shows cryo-TEM micrographs of an aramid amphiphile (OEG-AA) with an oligo(ethylene glycol) head group. The amphiphile spontaneously forms nanoribbons in water with 7.0 nm widths, 4.0 nm thickness, and lengths exceeding several micrometers. Both width and edge views are observed in Supplementary Fig. 24.

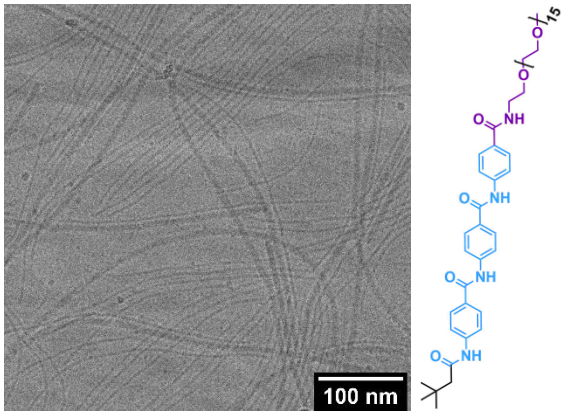

Supplementary Fig. 24. Representative Cryo-TEM image of an aramid amphiphile with a 15-mer oligo(ethylene glycol) head group, OEG-AA.

S3c. X-ray scattering

SAXS profiles of AA nanoribbons best fit to a core-shell lamellar model, which describes a lyotropic lamellar phase with head and tail group domains of different scattering length densities (SLDs).[28,29] Estimates for the SLDs of the hydrated hydrophilic head group domain (9.40×10^{-6} Å^{-2}) and the aramid-containing hydrophobic domain (11.13×10^{-6} Å^{-2}) were calculated based on the molecular formulae and input into SasView software. The solvent SLD (water) is 9.44×10^{-6} Å^{-2}. The model was adjusted to the appropriate scale and background, and fit for thickness of the two domains. The following models were

also attempted for fitting: lamellar, cylinder, flexible cylinder, core-shell cylinder*, parallelepiped, and core-shell parallelepiped*. Fits marked with an asterisk (*) allow for differing SLDs between the head and tail group domains. Despite a careful consideration of input parameters, each of these models, other than the lamellar model, fit to non-physical geometries based on Cryo-TEM images of the AA nanoribbons. In addition to the geometry of the amphiphilic nanostructures, the SAXS line shape can be affected by nanostructure aggregation, concentration, orientation/alignment, and dispersity, and instrument resolution. However, we still find this fitting useful as an indication of nanostructure geometry, complementary to other characterization techniques. From this fitting, the hydrophobic core was found to be 2.8 ± 0.1 nm and the combined hydrophilic head group thickness was found to be 1.1 ± 0.4 nm, for a total bilayer thickness of 3.9 ± 0.5 nm. The higher error in the hydrophilic region is likely due to its similar SLD as the solvent. The lamellar fits shown in Figure 2 and Supplementary Fig. 25 support that the nanoribbons adopt a rectangular cross-section as schematically illustrated in Figure 1, surrounded by a flexible, hydrated head group domain.

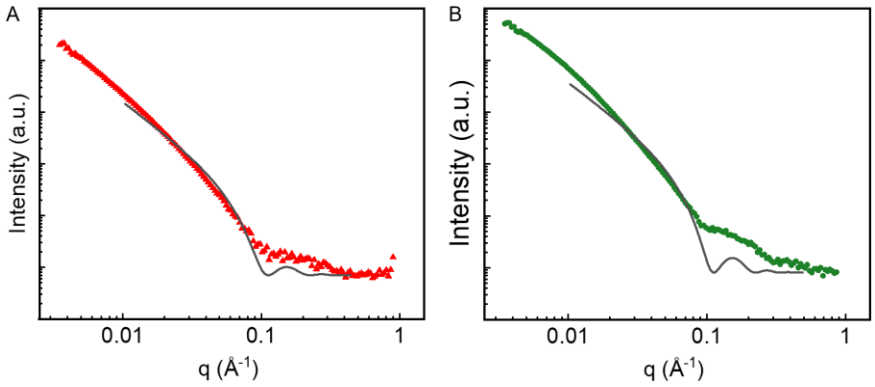

Supplementary Fig. 25. Lamellar fits (gray lines) to aqueous SAXS of (**A**) compound **1** (in red) and (**B**) compound **2** (in green) designates bilayer thicknesses of 3.9 nm for each nanoribbon.

SAXS of all aramid amphiphile assemblies was captured at 80 °C to probe the thermal stability of the nanostructures. Capillaries were heated from room temperature to 80 °C at 10 °C/min in a Linkam TMS600 heating stage and synchrotron SAXS profiles were captured at 0 min., 5 min., and 10 min. after reaching 80 °C. No changes in assembly morphology were observed under these conditions, as shown in Supplementary Fig. 26. All profiles are background subtracted using a water-filled capillary which underwent the same heating. The lower signal-to-noise observed in SAXS of compounds **1** and **2**, compared to compound **3**, is due to their limited solubility.

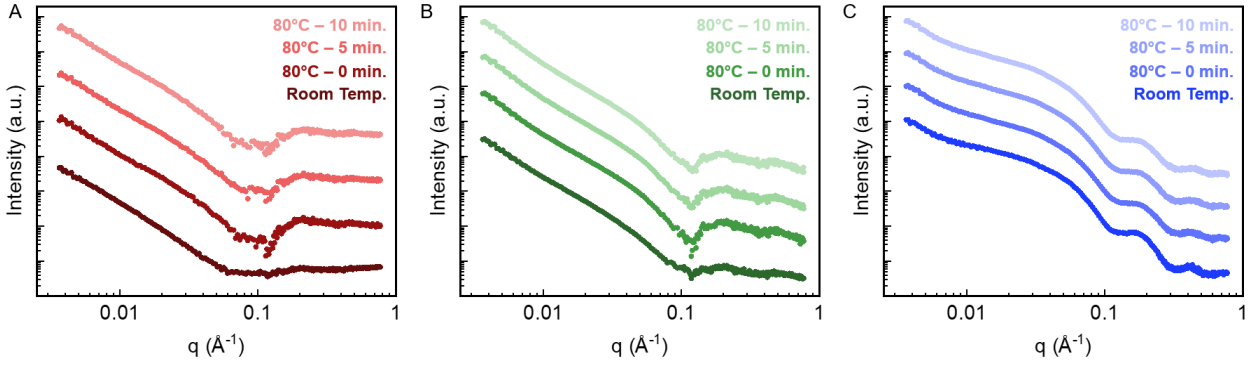

Supplementary Fig. 26. Aqueous SAXS of (**A**) compound **1**, (**B**) compound **2**, and (**C**) compound **3** shows no change in nanostructure morphology upon heating to and equilibrating at 80 °C. The significantly higher solubility of compound **3** results in SAXS profiles with stronger signal than compounds **1** and **2**.

VESTA software was used for simulating the X-ray diffraction peaks shows in Figure 5c. In this simulation, the space group 26: *P*mc2$_1$ of poly(*p*-benzamide) is considered as the most relative packing structure in aramid nanoribbons due to the constraint of the parallel amide bonding from the tri-aramid domain[34]. Further, reversing of the intensities for the two most significant peaks is observed when the thread is tilted on the X-ray beam axis. This observation indicates the two significant peaks correspond to orthogonal planes with a common intersection along the thread direction, and the assumption of the space group is confirmed. The black dotted lines of simulated peak position in Figure 5c and Supplementary Fig. 27 are generated from the unit cell with a = 7.22 Å, b = 5.05 Å and c = 11.10 Å parameters.

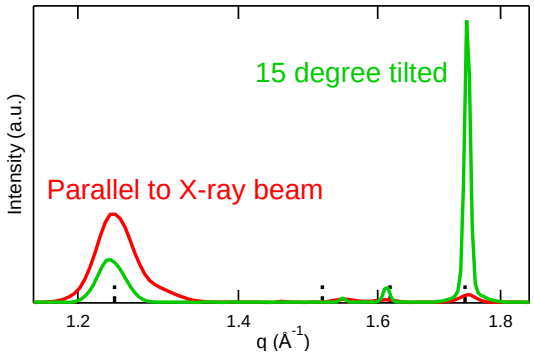

Supplementary Fig. 27. 1D-WAXS scattering profile of meridional axis with tilting on the X-ray beam direction.

S3d. Atomic force microscopy

Atomic force microscopy (AFM) of compound **3** nanoribbons deposited onto a mica substrate is shown in Supplementary Fig. 28.

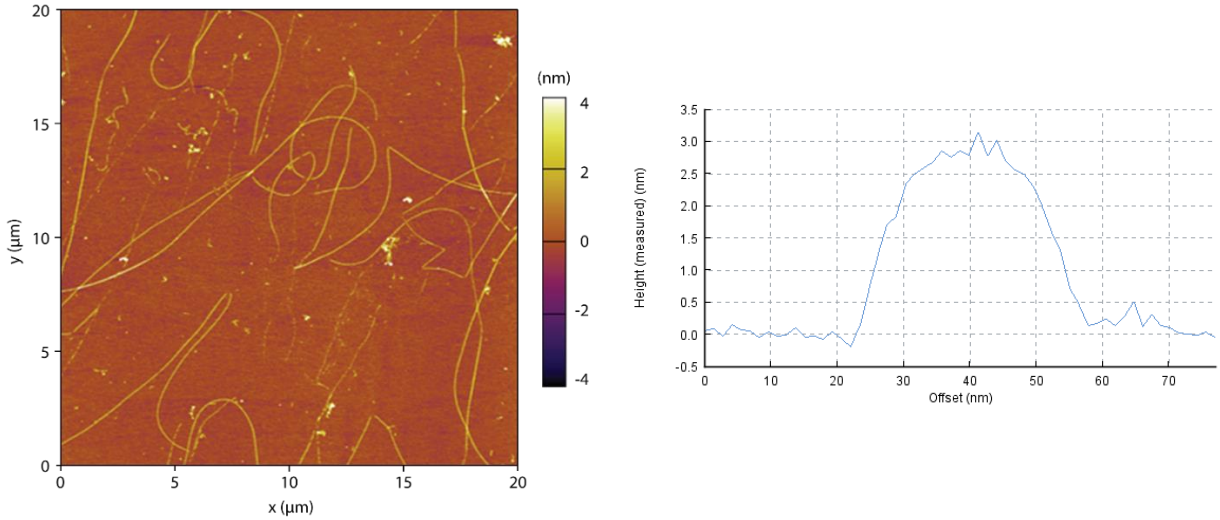

Supplementary Fig. 28. A representative AFM profile of compound **3** nanoribbons deposited on mica illustrates nanoribbon lengths up to 20 µm as determined by ImageJ analysis. A sample nanoribbon height profile is shown. AFM nanoribbon cross-section analysis reveals heights of 3.7 ± 0.5 nm (average over height measurements of 61 nanoribbons). Nanoribbon widths are not extracted from AFM due to tip convolution.

S3e. Scanning electron microscopy

Cast Films

We observed the hierarchical structure of AA threads by SEM (Supplementary Fig. 30). Striations along the thread axis of the dried threads are consistent with long-range alignment of nanoribbon bundles resulting from the shear alignment process.

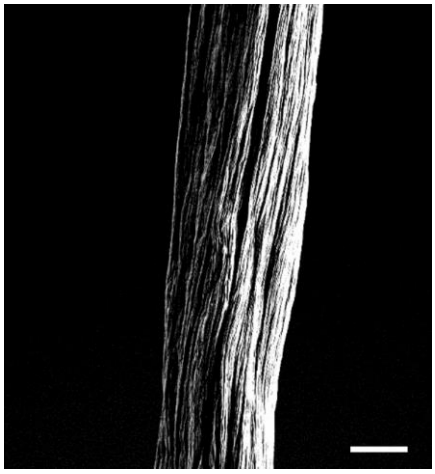

Supplementary Fig. 29. SEM of a 20 μm-diameter nanoribbon thread shows long-range alignment of nanoribbon bundles (scale bar, 10 μm).

S3f. Förster resonance energy transfer

EDANS and DABCYL serve as a typical Förster resonance energy transfer (FRET) pair with a Förster radius of 3.3 nm[39]. When the donor and quencher approach the Förster radius, energy transfer from the donor to the quencher results in a reduction of fluorescence intensity through vibrational relaxation pathways. Therefore, decreases in fluorescence intensity correlate to molecular exchange between adjacent nanoribbons (Figure 2D-E).

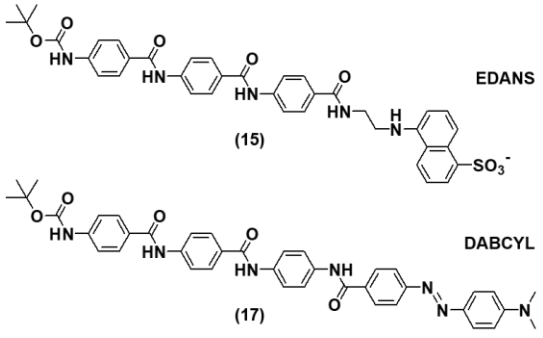

Supplementary Fig. 30. EDANS and DABCYL-based aramid amphiphiles used in the FRET study.

As a control, completely mixed co-assemblies of amphiphiles labeled with both a donor fluorophore and dark quencher show a 76% reduction in fluorescence intensity relative to assemblies labeled solely with the fluorophore (Supplementary Fig. 31).

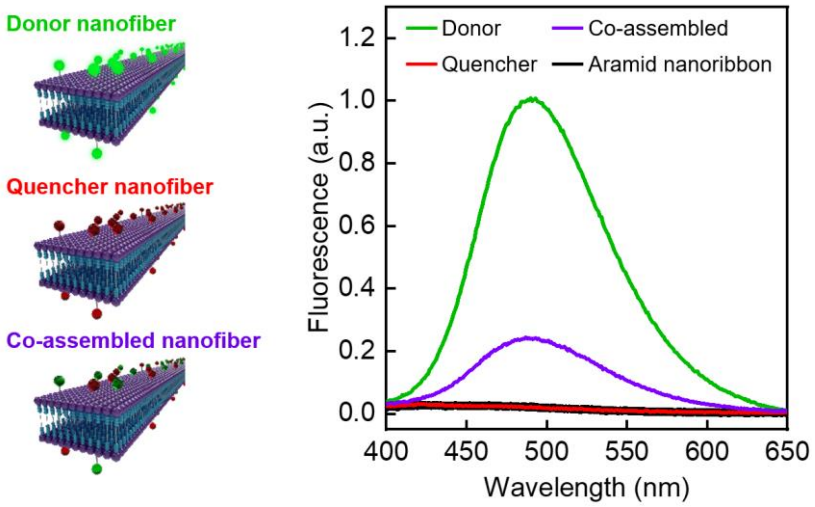

Supplementary Fig. S31. The fluorescence intensity of nanoribbons labeled with the FRET donor EDANS is quenched by 76% when co-assembled with FRET quencher DABCYL.

S3g. Stiffness determination by topographical analysis of nanoribbon contours

Sample preparation: Compound **3** was chosen for analysis by atomic force microscopy (AFM) because of its high solubility and favorable surface interaction with AFM substrates. DI water was added to a lyophilized sample of **3** to reach 30 mg/mL. A sonicator bath was used to accelerate self-assembly. After 24 h at room temperature, the suspension was diluted to 0.03 mg/mL and deposited on a clean glass surface. The glass substrate was prepared through cleanings with DI H_2O and ethanol, drying with stream of N_2 (g), and activation by UV/ozone treatment. After 5 min of incubating the nanoribbon suspension on the clean glass, the surface was rinsed with DI water and used directly for AFM imaging.

Experimental details: AFM images (Supplementary Fig. 32) were used to determine the persistence length and Young's modulus of the ribbons. Fluctuations of ribbon shape are statistically processed using the Easyworm software tool[43], which traces parametric splines to the contours of many ribbons of the same sample (in this experiment, n = 29 ribbons). Parametric splines store the $x - y$ coordinates of all the knots along the ribbons. Each combination of two knots gives a secant length L, and the midpoint of this secant deviates from the ribbon contour by a distance δ. The persistence length P is then obtained by least-square fitting the data to the worm-like chain model for semi-flexible polymers, $< \delta^2 > = L^3/(48 \times P)$, for ribbons equilibrating in 2-D. The persistence length reflects how much a ribbon bends as a result of thermal fluctuations. A higher persistence length of a ribbon corresponds to a lesser change in orientation over a given distance along its contour. The flexural rigidity F is the result of scaling the persistence length to the thermal energy according to $F = P \times k_B T$. Finally, the Young's (elastic) modulus E is obtained using $E = F/I$, where I is the area moment of inertia, which reflects the resistance to bending of a cross-section. For the circular cross-section observed in AFM measurements, the moment of inertia, $I = \pi \cdot d^4/64$, where d is the ribbon diameter. Heights of each nanoribbon were estimated by analysis of nanoribbon cross-sections observed in the AFM images. The AFM height measurements are consistent with cryo-TEM and SAXS measurements, and therefore we use $d = 3.7 \pm 0.5$ nm to calculate I.

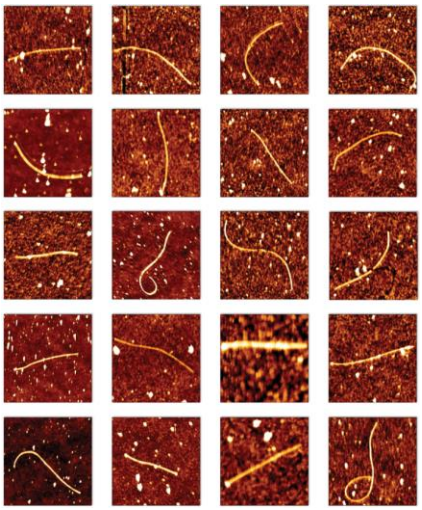

Supplementary Fig. 32. Contour traces of AFM images of AA nanoribbons, a representative set of which are shown here, were used for determining nanoribbon stiffness by statistical topographical analysis. Image dimensions are 1 μm x 1 μm.

S3h. Yield strength determination by sonication-induced scission

We measure the yield (tensile) strength σ* by using a sonication-induced fibril scission technique, as detailed in our previous work[48]. In short, sonication creates collapsing cavitation bubbles, causing fluid velocity fields to trap fibrils and exert shear forces on them. This leads to fibril extension in opposite directions and mechanically-induced rupture at the site of highest stress. The model developed by Huang et al. implies that the forces exerted on the fibril decrease dramatically with the fibril length[44]. Hence there is a threshold length L_{lim} below which a fibril of a given cross-section will not break anymore. We plot the length of hundreds of fibril fragments as a function of their cross-sectional size (see Supplementary Fig. 33), and derive σ from the relationship[44]:

$$L_{\mathrm{lim}} = \alpha C \sqrt{\sigma} \qquad (1)$$

where $\alpha = 7.10^{-4}$ is a prefactor that depends on the experimental conditions, and C reflects the cross-sectional size of the fibril fragments. For a rectangular cross-section fibril with long edge w (i.e. TEM width), and short edge h (i.e. AFM height), it is given by[48]:

$$C = \left[\frac{\gamma}{2w^2}\left[\left(\ln\left(\gamma + \sqrt{\gamma^2 + 1}\right) + \ln(\gamma^{-1} + \sqrt{\gamma^{-2} + 1})\right]\right]^{-1/2} \qquad (2)$$

where $\gamma = w/h$ is the aspect ratio. After prolonged sonication time, fibril length distribution reaches a plateau and the size of fragments that belong to a sample fall in a "terminal range" defined by $\left[{L_{lim}}/{2}, L_{\mathrm{lim}}\right]$. However, we expect an even broader distribution of fragment lengths L, because both the cross-sectional area and intrinsic strength can vary. This broadening of the terminal range is considered by determining the lines of best fit from the extremities of the distribution[48]. We represent the extremities by the 5–10 data points corresponding to the smallest and longest aspect ratios L/C (see the black dots in Supplementary Fig. 34), discarding obvious outliers. The lowest slope s reflects the low boundary of the shortest terminal range (*i.e.* the smallest aspect ratio), and the highest slope S exposes the high boundary of the longest terminal range (*i.e.* the longest aspect ratio). The shortest and longest terminal ranges are thus defined by intervals $[s, 2s]$ and $[S/2, S]$, respectively. L_{lim} is the averaged top of any terminal range given by:

$$\frac{L_{\mathrm{lim}}}{C} = \frac{2s + S}{2} \pm \frac{2s - S}{2} \qquad (3)$$

Combining the results of Eq. 2 with Eq. 1 we obtain the tensile strength σ. This method is particularly solid to reveal at least the position of the lower edge of the terminal distribution, which corresponds to the lowest possible strength of the fibril sample. Using the absolute error ± (2s – S)/2 provides a simple way to account both for any experimental source of error and for the strength variability within a given sample. In this study all fibril fragments have a similar cross-sectional area, with w = 6.0 ± 1.3 nm and h = 3.1 ± 0.5 nm. Consequently, most fragment lengths are distributed in one single terminal range $\left[\frac{L_{\mathrm{lim}}}{2}, L_{\mathrm{lim}}\right]$, as displayed in the histogram of the fragment length distribution (see Supplementary Fig. 33). In order not to overestimate the strength, we use a cut-off value to discard all fibril fragments with L > 134 nm. These fragments most likely escaped sonication-induced breakage because the initial fibril concentration was relatively high (~0.5 mg/mL); as a result, their lengths did not end up into the terminal range. To calculate the cut-off, we assume the most prominent peak of the distribution to correspond to $L_{\mathrm{lim}}/2$ and fit a Gaussian to that peak, which gives $L_{\mathrm{lim}}/2$ = 55 ± 12 nm for TEM. We thence estimate L_{lim} = 110 ± 24 for TEM and use it to derive the cut-off.

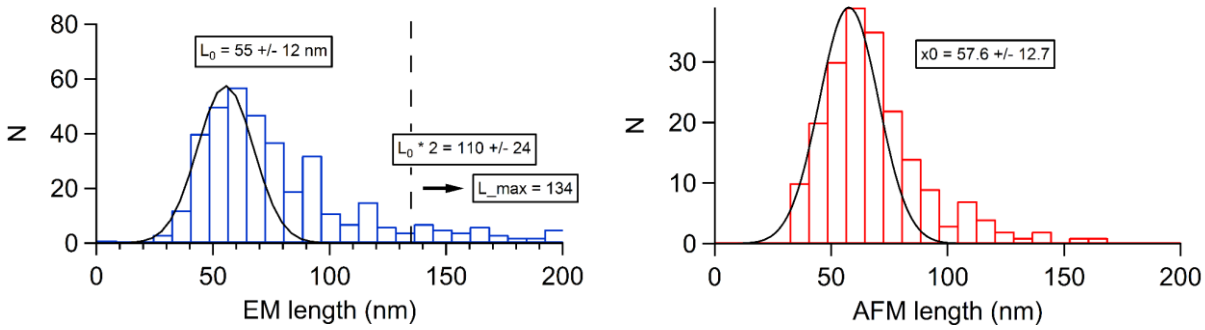

Supplementary Fig. 33. The distribution of fragment lengths after sonication-induced scission of nanoribbons of **3** as measured by (**A**) TEM and (**B**) AFM.

Here the fragment lengths were independently estimated in both TEM and AFM measurements. Both techniques give similar results, also translating in similar strength values. For the determination of the cross-sectional parameter C, we used the AFM-determined mean height of the fibril fragments $h = 1.96 \pm 0.55$ nm in the analysis of the TEM data (Supplementary Fig. 33a), and we used the TEM-determined mean width of the fibril fragments $w = 6.0 \pm 1.3$ nm in the analysis of the AFM data (Supplementary Fig. 33b). Note that the mean AFM height of the fibril fragments is lower than that of non-sonicated fibrils, possibly because non-sonicated fibrils are higher-order assemblies and sonication leads to partial disassembly of the several protofilaments that form a "mature" fibril. The highest and lowest lines in this plot identify L_{lim} and the smallest fragments produced by sonication, respectively, and the yellow region considers a broadening of these bounds due to variations in cross-sectional area and intrinsic strength.

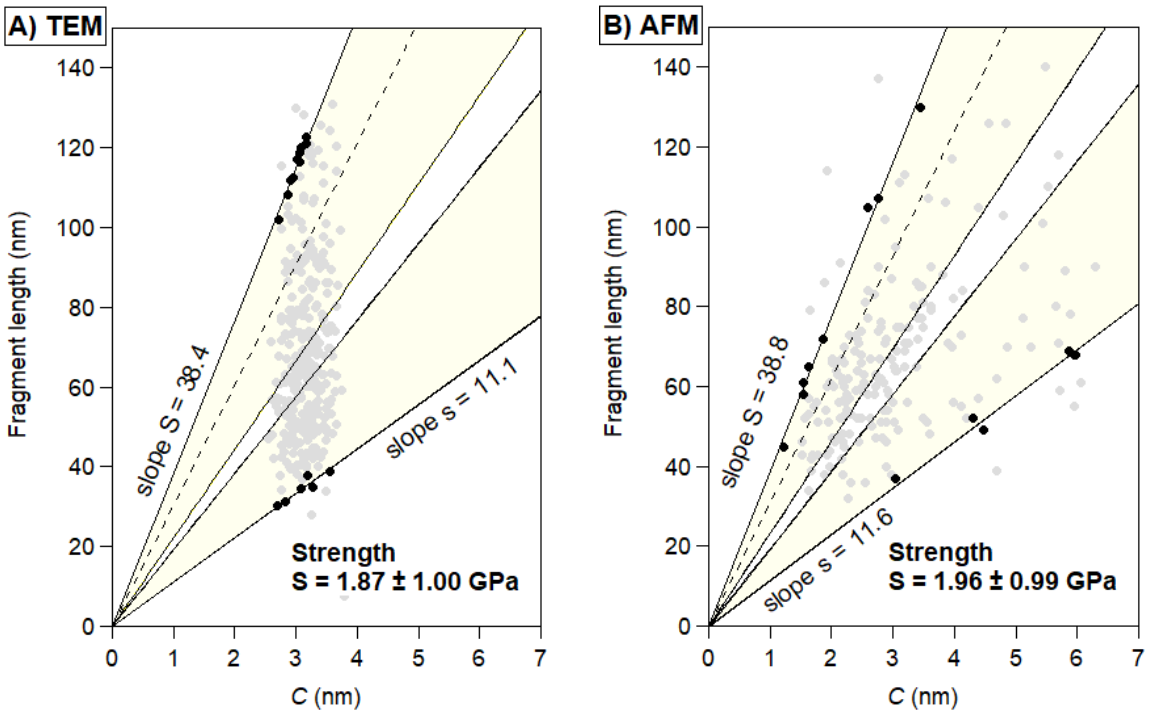

Supplementary Fig. 34. Yield strength analysis of nanoribbons of **3** from sonication-induced scission identifies strengths of (**A**) 1.87 ± 1.00 GPa based on TEM and (**B**) 1.96 ± 0.99 GPa based on AFM analysis of the nanoribbon fragments, showing a close convergence between the two techniques.

S3i. Tensile strength testing of macroscopic AA nanoribbon threads

Tensile testing was performed to obtain Young's modulus and elongation at break values for AA threads formed with sulfate or methanedisulfonate counterions. These results from the mechanical tests are summarized in Supplementary Figs. 35 and 36 below for n = 6 threads per counterion.

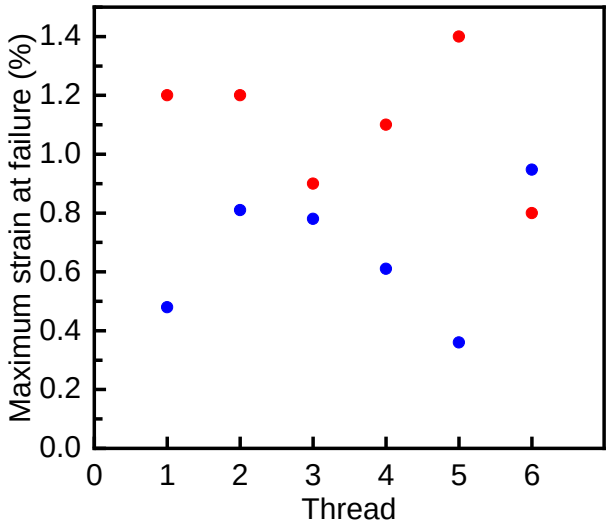

Supplementary Fig. 35. The Young's elastic modulus for sulfate (blue) and methanedisulfonate (red) AA threads is extracted from their tensile test curves.

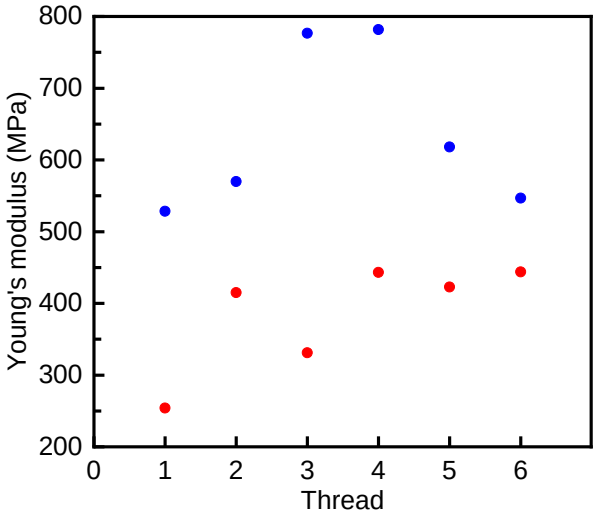

Supplementary Fig. 36. The elongation at break for sulfate (blue) and methanedisulfonate (red) AA threads is extracted from their tensile test curves.